Probing neutron-star matter in the lab: Similarities and differences between binary mergers and heavy-ion collisions

Elias R. Most,[1,2,3] Anton Motornenko,[4,5] Jan Steinheimer,[5] Veronica Dexheimer,[6] Matthias Hanauske,[4,5] Luciano Rezzolla,[4,5,7] and Horst Stoecker[4,5,8]

[1]*Princeton Center for Theoretical Science, Princeton University, Princeton, New Jersey 08544, USA*
[2]*Princeton Gravity Initiative, Princeton University, Princeton, New Jersey 08544, USA*
[3]*School of Natural Sciences, Institute for Advanced Study, Princeton, New Jersey 08540, USA*
[4]*Institut für Theoretische Physik, Goethe Universität, D-60438 Frankfurt am Main, Germany*
[5]*Frankfurt Institute for Advanced Studies, Giersch Science Center, D-60438 Frankfurt am Main, Germany*
[6]*Department of Physics, Kent State University, Kent, Ohio 44243, USA*
[7]*School of Mathematics, Trinity College, Dublin 2, Ireland*
[8]*GSI Helmholtzzentrum für Schwerionenforschung GmbH, D-64291 Darmstadt, Germany*

(Received 31 January 2022; revised 17 December 2022; accepted 14 February 2023; published 27 February 2023)

Binary neutron-star mergers and heavy-ion collisions are related through the properties of the hot and dense nuclear matter formed during these extreme events. In particular, low-energy heavy-ion collisions offer exciting prospects to recreate such extreme conditions in the laboratory. However, it remains unexplored to what degree those collisions can actually reproduce hot and dense matter formed in binary neutron star mergers. As a way to understand similarities and differences between these systems, we discuss their geometry and perform a direct numerical comparison of the thermodynamic conditions probed in both collisions. To enable a direct comparison, we employ a finite-temperature equation of state able to describe the entire high-energy phase diagram of quantum chromodynamics. Putting side by side the evolution of both systems, we find that laboratory heavy-ion collisions at the energy range of $E_{\rm lab} = 0.4$–$0.6A$ MeV probe (thermodynamic) states of matter that are very similar to those created in binary neutron-star mergers. These results can inform future low-energy heavy-ion collisions probing this regime.

DOI: 10.1103/PhysRevD.107.043034

I. INTRODUCTION

Quantum chromodynamics (QCD), the theory of strong interactions, predicts that matter at densities and temperatures found in binary neutron star mergers (BNSMs) and relativistic heavy ion collisions (HICs) consists of the same particles that obey the same interactions despite drastic differences of system sizes. Although hot dense matter is predicted to appear in a plethora of different states under different conditions [1–5], in the laboratory it is only possible to measure the final hadronic states that are emitted from the late stages of HICs. This is what we refer to as nuclear matter, not only protons and neutrons that at low energy are clustered into nuclei, but also hyperons (that contain strange quarks), negative parity states, and mesons. The life-time of HICs is so short, that full evolution conditions are problematic to reconstruct. Indirect observations of the quark-gluon plasma (QGP) were done in high-energy collisions [6–10], though the details of such a state and the transitions that lead to it from nuclear matter and vice-versa are not yet known to great detail. Current state-of-the-art lattice QCD calculations of thermodynamic properties at vanishing baryon density (which corresponds to the fireball created in the highest-energy HICs, with the same number of particles and antiparticles for zero net-baryon density) suggest that the deconfinement transition from hadronic matter to the QGP appears smoothly [11–13], i.e., there is no sharp boundary between the states. At finite, as well as high baryon densities, the phase structure is still rather unconstrained, and the existence of a first order phase transition, i.e., with a sharp boundary between the phases, is not ruled out. Verification of such a possibility is one of the top priority research tasks at several running and upcoming HIC facilities [14–22].

Since the first gravitational detection of a BNSM in 2017, GW170817 [23], we have already employed the knowledge gained from mergers to improve our understanding of cold and dense nuclear matter by placing strong constraints on the neutron-star maximum mass [24–27] and typical radii and tidal deformabilities [28–44]. In a similar manner, HICs have been suggested to provide complementary constraints. Using flow studies, Ref. [45] (see also [46]) has extracted isotropic pressure constraints from low-energy HICs. These have recently been employed to

(jointly with multimessenger constraints) derive bounds on the cold dense matter EoS [47]. More fundamentally, this raises the question of what complementary information about hot and dense matter BNSMs can provide compared with HIC, given that both systems feature non-negligible temperatures. How similar is stellar nuclear matter to that produced in a HIC? In particular, future BNSM events might open up the possibility to complement the experimental investigations of the short-lived microscopic nuclear matter created in HICs by detecting signals from the longer-lived macroscopic amount of (hot) nuclear matter formed in the merger. The main signatures would potentially be contained in the postmerger gravitational-wave emission [48–57], making this question a prime target for next-generation gravitational wave facilities [58–60]. On the HIC side, recent evidence of the formation of hot matter at several times saturation density in low-energy HICs was reported by the HADES collaboration [19], conditions potentially resembling those present in a BNSM. However, in the absence of a direct and meaningful comparison between these two systems, it is far from clear exactly how similar the conditions probed in HICs and BNSMs really are.

Motivated by these claims, we aim to answer the following question: *Can experiments such as [19] reproduce BNSM geometry and thermodynamic conditions, and what experimental "settings" are necessary? How does gravity alter the outcome of macroscopic collisions, and what is actually meant by similar conditions in both cases?* To answer these questions, we perform a systematic and direct side-by-side comparison of geometry and thermodynamic properties in HICs and BNSMs. This is done by means of relativistic hydrodynamics simulations of both systems. Crucially, we employ the same realistic microphysical EoS model, describing the entire high-energy QCD phase diagram, and the similar numerical methods to make the comparison as meaningful as possible. Introducing a quantitative figure of merit—the entropy production during the collision—to assess the similarity of the matter formed in both collisions, we derive bounds on the beam energies needed to probe BNSM-like conditions in laboratory HIC experiments.

II. METHODS

In this work, we aim to compare nuclear matter in HICs and BNSMs by means of relativistic hydrodynamics simulations. To enable a meaningful comparison, we need to ensure two things. First, the microphysics needs to be the same in both cases, so that we can map the thermodynamic conditions present in one system to the other. Second, the numerical methods needs to be both reliable and comparable to ensure that effects such as shock heating are captured to the same degree in both simulations.

A. Microphysical model

The EoS used to describe both systems should be derived from a consistent model that is valid across the entire high-energy QCD phase diagram, covering the large range of temperatures and densities involved, in addition to describe different fractions of isospin and strangeness. Additionally, such a model must be able to reproduce current constraints for compact stars and collider conditions (e.g., from Lattice QCD). More precisely, we consider constraints from cold compact stars (e.g., [61–68]), properties of symmetric nuclear matter [47,69–81], and high-temperature QCD constraints at vanishing and low density, including a consistent description for chiral-symmetry restoration and quark deconfinement reproducing data from lattice QCD [11–13,82], perturbative QCD [83,84], and high-energy collider experiments [85].

Addressing all of the above, we make use of the chiral mean field (CMF) model, which is based on the three-flavor chiral Lagrangian for hadronic matter first introduced in [86] and extended to describe neutron stars in [87]. Our version of the CMF model [88] uniquely incorporates a full list of QCD degrees of freedom, including, besides protons and neutrons, hyperons, their parity partners, and the full list of hadronic resonances (strange and nonstrange baryons and mesons) as found in the particle data book [89]. In addition, the thermal contribution of deconfined quarks and gluons is added as in the Polyakov-Nambu-Jona-Lasino approach [90–94]. Together with the electrons this corresponds to the most complete set of QCD degrees of freedom available for the high density equation of state. A more detailed description on the CMF model and its contents can be found in e.g., [95]. In addition, a low density model that includes the description of nuclei was gradually matched to the CMF-EoS, for the BNSM simulations, below $10^{-2}n_{\rm sat}$. See Ref. [96] for details on the matching and the low-density EoS.

Our version of the CMF model reproduces a crossover transition for deconfinement at finite and zero density (as determined by lattice QCD) [95,97], and providing a good description for hadrons in medium, nuclei, nuclear matter and neutron stars [88,98]. The latter includes reproducing $M > 2M_\odot$ stars and stars with radii within LIGO-Virgo and NICER allowed regions. The model produces a nuclear ground state with realistic properties: saturation at (baryon number) density $n_{\rm sat} = 0.15\ {\rm fm}^{-3}$, binding energy per nucleon $E_0/B = -15.2$ MeV, symmetry energy $S_0 = 31.9$ MeV, symmetry energy slope $L = 57$ MeV, and incompressibility $K_0 = 267$ MeV. This comprehensive approach allows to calculate the EoS of nuclear matter created in HICs and in BNSMs, without introducing additional ambiguities due to the use of (potentially inconsistent) different EoS in the two regimes. In addition, for BNSMs we include a free gas of electrons to the EoS to maintain electric charge neutrality. We calculate numerical

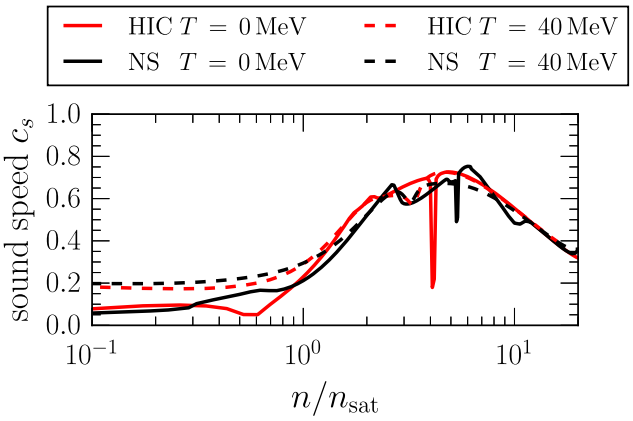

FIG. 1. Isothermal sound speed, c_s, in the CMF equation of state for different scenarios. Black lines: Neutron star matter, including electrons in beta equilibrium and fulfilling charge neutrality. Red lines: Heavy ion collision matter with zero isospin and strangeness conservation. The solid lines correspond to the speed of sound at $T = 0$ MeV and the dashed lines to $T = 40$ MeV. A maximum in the speed of sound is clearly visible for all scenarios despite differences in the details due to the varying chemical composition.

tables of the temperature and density, as well as isospin dependence (e.g., difference between the amount of neutrons and protons) of the CMF-EoS, which are then implemented in the hydrodynamical models.

In order to put the following simulation results into context of the EoS and to justify our assumption that HICs and BNSMs can be used complementary to study the QCD EoS, the speed of sound from the CMF model is presented in Fig. 1 (see also Refs. [42,99,100] for recent studies on the general properties of the sound speed in neutron stars). In particular, we show the isothermal speed of sound, c_s, as function of the baryon density at some relevant fixed temperatures of $T = 0$ MeV and $T = 40$ MeV. In both scenarios, we also compare the CMF results for either neutron star matter, including electrons in beta-equilibrium, as well as HIC matter which is isospin symmetric and where strangeness is conserved (number of strange particles matches the number of strange antiparticles). The last two conditions are a consequence of the very short lived character of HICs. Noticeably, the overall structure of the EoS is very similar for these two extreme cases: a clear maximum in the speed of sound is observed for 4-6 times saturation density (see also Ref. [101] for a more general discussion on the maximum of the sound speed in neutron stars). Both the decrease from the maximum at high densities and the oscillations are linked to the appearance of new degrees of freedom.

While the details of the curves show clear differences due to the different chemical compositions of the systems, it is important that only the similarities allow us to study the properties of the QCD EoS in these very different microscopic vs macroscopic scenarios.

B. Numerical methods

The other critical component of our study is the dynamical description of both BNSMs and HICs using relativistic hydrodynamics, which essentially provides conservation laws for the baryon current and the stress-energy tensor (see, e.g., [102] for a review). More specifically, we assume that the systems are (to lowest order) described as compressible perfect fluids. Although other hydrodynamic implementations, incorporating viscous effects or even a microscopic transport description of HICs are possible, it was shown that, if the same EoS is used, the HIC system dynamics and entropy production, as calculated with the hydrodynamical approach, are quite similar to the complementary predictions of nonequilibrium transport models [103,104], see also [105–113]). Similarly, in the case of BNSM, viscous effects largely arise from modified Urca interactions [114,115]. While these can lead to small changes in the gravitational wave emission, their impact on the thermodynamics is subdominant. However, they might play a fundamental role in adjusting the isospin fraction of dense matter [114], which we ignore in the comparison presented here. In spite of that, perfect hydrodynamics is perfectly able to capture entropy production in the compressional regime of the flow by means of local Rankine-Hugoniot shock junction conditions [116]. In fact, a recent study [114] has shown that (microphysical) viscous entropy production in BNSMs is of the order of 0.1/baryon (in natural units).

The dynamical description of the evolution of both BNSMs and HICs is kept on the same footing by evolving in time the equations of relativistic hydrodynamics on a three-dimensional grid for both scenarios, but employing different numerical implementations. In the case of HICs, we use the Frankfurt SHASTA code [117,118] with a uniform grid spacing $\Delta x = 0.2$ fm and time step $\Delta t = 0.08$ fm$/c$. Our HIC initial state consists of two drops of cold zero temperature nuclear matter colliding head-on with Lorentz-contracted Woods-Saxon density distributions, propagating toward each other with relativistic speed in the center-of-mass frame of the collision. For each energy, a near central collision of two gold nuclei (Au) is computed at fixed offset "impact parameter" $b = 2$ fm at lab energies of $E_{\rm lab} = 450$ and $600A$ MeV per nucleon, corresponding to those available to the HADES collaboration for low-energy HICs at GSI [19]. For our BNSM simulations, in addition to the equations of general-relativistic hydrodynamics [116], we need to solve Einstein's equations in the conformal Z4 formulation [119–122]. The full set of equations is evolved using the Frankfurt/IllinoisGRMHD (FIL) code [123–125]. Making use of nested box-in-box mesh refinement [126], our simulations use 7 levels of refinement with the highest resolution of $\Delta x = 250$ m and outer box size of 1500 km. The adopted resolution has been shown to be sufficient within the context of this work [50,124]. The initial conditions are

two equal-mass with total masses of 2.6 and $2.8M_\odot$ [127]. We neglect spins in line with the assumption that most systems are essentially irrotational at merger [128].

III. RESULTS

In the following, we provide a comparison of low-energy HICs with BNSMs. Specifically, we focus on the geometry and thermodynamic properties of the matter probed in each system. That is, because a full comparison of the flow structure for both systems is complicated by the fact that BNSMs have net angular momentum and are gravitationally bound. However, thermodynamic quantities in the local rest-frame of each fluid element in the collision remain meaningful. Since in the absence of physical viscosity the flow is isentropic, the entropies S per baryon A can serve as a meaningful tool to compare the flows in both cases. Following along those lines, we proceed in three stages. First, we provide an overview of the collision dynamics in Sec. III A. Second, in Sec. III B we perform a detailed assessment of the entropy per baryon evolution in both cases. Finally, we perform a direct comparison of the phase-diagram coverage for different beam energies and BNS masses in Sec. III C, establishing in which cases low-energy HICs can reproduce BNSM-like conditions.

A. Overview of collision dynamics

In the following, we give an overview of the collision dynamics of both systems. For a HIC, the two gold nuclei approach each other head-on along the z-direction, with relative velocities $v \gtrsim 0.5c$ and only a small offset b along the transverse x-axis. This produces dense hot matter with the longest lifetime and highest compression (highest density) at a given beam energy. Once the two nuclei make contact, the cold nuclear matter in the center is rapidly heated and entropy is generated [103,129]. Once both incoming nuclei are compressed into a single fireball, matter starts to rapidly expand along an isentropic trajectory until diluting so much that the hydrodynamic picture is no longer valid and freeze out occurs. In our simulations, this corresponds to cells at roughly $n \sim \frac{1}{2} n_{\rm sat} \approx 0.08$ fm^{-3}. At this point in the emitted nuclear matter will start to form clusters with important consequences for experimental studies of the EoS. Recent work has shown, that the maximum compression and entropy production from shock heating are rather insensitive to viscous corrections, when adopting relatively low beam energies as considered in this work [130]. This allows us to safely neglect such corrections in the present comparison.

In the case of BNSs, the two stars are initially on a quasicircular orbit, but the emission of gravitational waves causes the two stars to collide (see, e.g., [131] for a review). Differently from a HIC, the collision is not head-on. First, the merger remnant retains a significant fraction of angular momentum [132]. Second, tidal forces deform the neutron stars prior to merger, with small-scale turbulence induced in the shearing interface between them (see, e.g., [133]). During the merger, the two stars are compressed to a few times $n_{\rm sat}$ and heated considerably, leading to supersonic velocities and the formation of shocks. This causes a steep increase in temperature and a local production of entropy, similar to a HIC.

The differences in the dynamics between BNSMs and HICs are shown in Fig. 2, where we report the temperature T (lower colormaps), the entropy per baryon S/A (upper colormaps), and the density (isocontours) for a BNS collision (top panels) and a Au + Au collision (bottom panels). Note in the top row that, in spite of similar geometry, the entropy production in BNSMs is limited to a narrow spatial range at the interface of the two stars, where the densities probed are below $2n_{\rm sat}$. The precise structure of the merger remnant and, hence, the compression of layers, is governed by the strong gravitational fields present. Even some time into the collision, the heating and production of entropy is confined to the original collision interface.

This is qualitatively different behavior from what happens in HICs, where, in the early phase of the collision, entropy production is also confined to a very thin ellipsoid in the narrow initial overlap of the two nuclei. However, in the course of the reaction, the compression causes the entire gold nucleus (show as the contour with $n \gtrsim \frac{1}{2} n_{\rm sat}$) to heat up. Another important difference is that, after the BNSM, most of the resulting object is gravitationally bound, while in the HIC case, the resulting remnant is an evanescent fireball of matter expanding isentropically at relativistic speeds. Finally, whereas in a BNSM, the overall rotation of the system and the conservation of the Bernoulli constant [134] leads to a redistribution of hot parts of the fluid, which ultimately settles down in a ring-like structure [134,135], the hot fireball produced in a HIC cools rapidly, during the fast, isentropic expansion, with the central region always being at the highest temperature.

To summarize, even though the details of the dynamical evolution of both systems appear dramatically different, and the description of these can be rather technical, it is important to note that the bulk properties of the hot systems created are actually very similar. We discuss them in more detail in the following.

B. Entropy evolution on micro- and macroscales

To exploit the similarities between BNSMs and HICs, we compare the collision dynamics of the two systems by identifying the most important initial properties that lead to the same bulk entropy per baryon in the collision, namely, the beam energy in the case of HICs and the total stellar gravitational mass in BNSMs. To illustrate this behavior, we directly contrast the evolution of the entropy per baryon in the two different systems. The detailed comparison is shown in Fig. 3 in terms of 1 + 1 spacetime diagrams. To

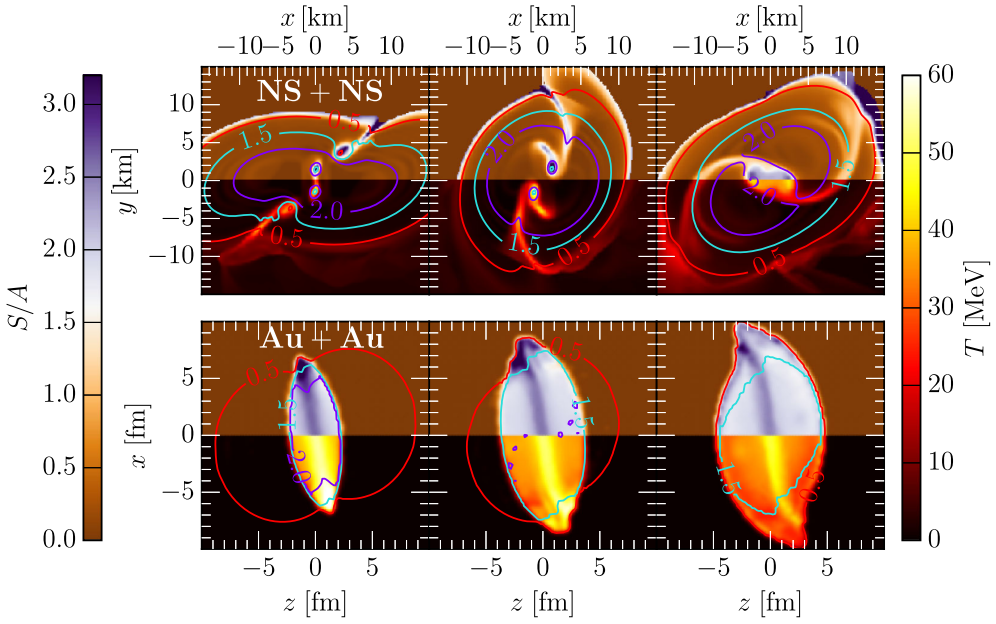

FIG. 2. Distributions of entropy per baryon S/A (upper color maps) and temperature T (lower color maps) for a BNSM (NS + NS) with total mass $M_{\rm tot} = 2.8M_\odot$ (top panels) and a Au + Au HIC at $E_{\rm lab} = 450A$MeV (bottom panels). Colored lines mark density contours in units of $n_{\rm sat}$. The snapshots in different rows refer to $t = -2, 0, +3$ ms before and after merger for the BNSM, respectively, and to $t = -5, 0, +5, \mathrm{fm}/c$ before and after the full overlap for the HIC.

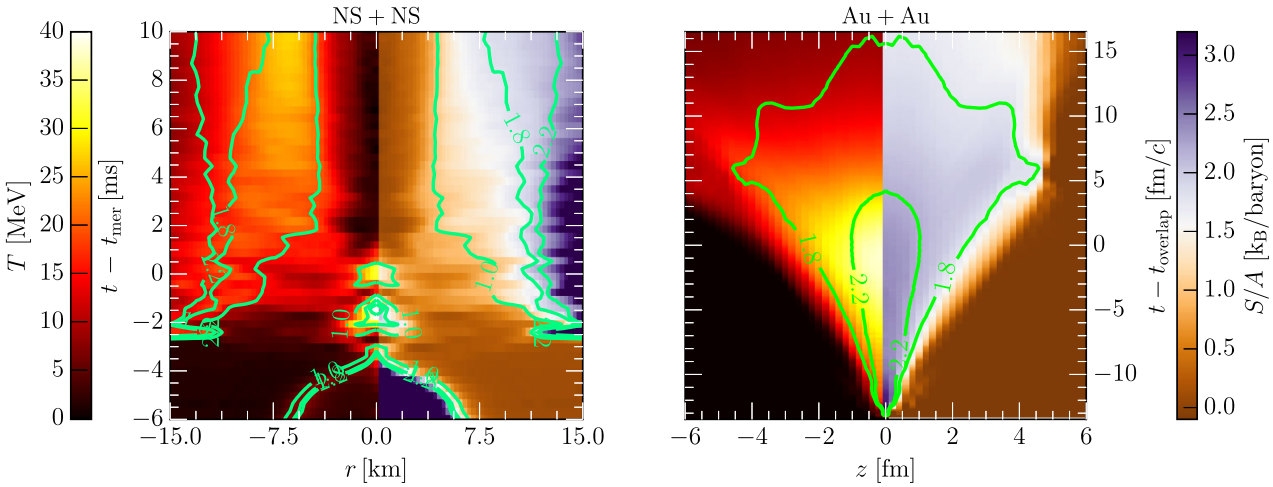

FIG. 3. Dimensionally reduced spacetime diagrams for the evolution of the temperature and entropy per baryon relative to the same BNSM (left panel) and HIC (right panel) presented in Fig. 2. The green contours correspond to lines of constant entropy per baryon S/A; only regions with density above freeze-out, $n > \frac{1}{2}n_{\rm sat}$, are shown for the HIC.

reduce the dimensionality of the collisions, we restrict to the equatorial (x, y) plane for the BNSM and average out the azimuthal dependence, so that $r := (x^2 + y^2)^{\frac{1}{2}}$. In the case of the HIC, the whole transverse dependence in the (x, y) plane is averaged out.

The left panel of Fig. 3 illustrates that before the collision the temperatures and entropies of the stars are low. Tidal interactions during the inspiral can lead to a mild heating of the outer layers of the stars, but this is negligible as compared to the shock temperatures reached in the merger [136]. At the time of the merger, i.e., $t \simeq -3$ ms,[1] regions of very high temperature and entropy per baryon are formed around r $\simeq 3$ km. Note that the merger remnant undergoes a significant thermodynamical evolution. The presence of

[1]The merger time is set when the gravitational-wave amplitude has its first maximum [137] a few milliseconds after the stellar surfaces have touched [138].

high angular momentum generates high shear flows despite of the fact that the two stars were initially assumed irrotational. These shear flows transport outward the temperature and the entropy, leaving a comparatively cold and dense core (see regions with $r \lesssim 3$ km) surrounded by a much hotter ringlike structure that remains stationary in time [139] ($4.0 \lesssim r \lesssim 7$ km). The temperature and density further decrease when moving to the outer regions of the remnant ($r \gtrsim 8$ km). A similar behavior is shown by the evolution of the entropy distribution, which exhibits a dense core with low entropy per baryon, surrounded by a hot ring with $S/A \simeq 1$–2. We caution that the precise values of temperatures and entropies being probed might critically depend on physics around saturation [140]. A detailed investigation with a broader set of currently unavailable EoS will be necessary to more precisely estimate this error budget in both systems.

The spacetime diagram for a HIC (right panel of Fig. 3) shows an ever increasing central-shock zone of high entropy per baryon and high-temperature dense matter produced from the initial collision, starting from $t \simeq -15$ fm$/c$ and up to the moment of full overlap of the two nuclei. Subsequently, the interpenetration stage of the two nuclei is over. Hence, the ellipsoid of arrested, hot, shock-heated, and compressed matter can expand freely forward and backward along the collision axes at $|z| > 4$ fm. The expansion of matter is essentially isentropic, with average entropies of $S/A \approx 2.5$.

When comparing the two panels in Fig. 3, it is important to note that there are striking analogies in the thermodynamics properties of the postcollision dynamics, but also that these are confined mostly to the merger phase. This is because the postcollision in a BNS is intrinsically different from that in a HIC: in the former case, strong gravitational fields lead to a remnant that is gravitationally bound and in a metastable equilibrium [133]. By contrast, the hot and dense matter produced in HICs is unbound and quickly expands into the surrounding vacuum.

C. Comparison in the QCD phase diagram

Figure 4 shows the spatial *and* temporal evolution of these systems in the QCD phase diagram in terms of the temperature and density of the various fluid cells. This is obtained by binning into the variable N, across the whole evolution and for both BNSMs and HICs, all fluid elements according to their temperature and density. This means that a higher N represents more regions that for longer timer have a given temperature and density. As a simplification, for BNS mergers we assume the equatorial plane dynamics

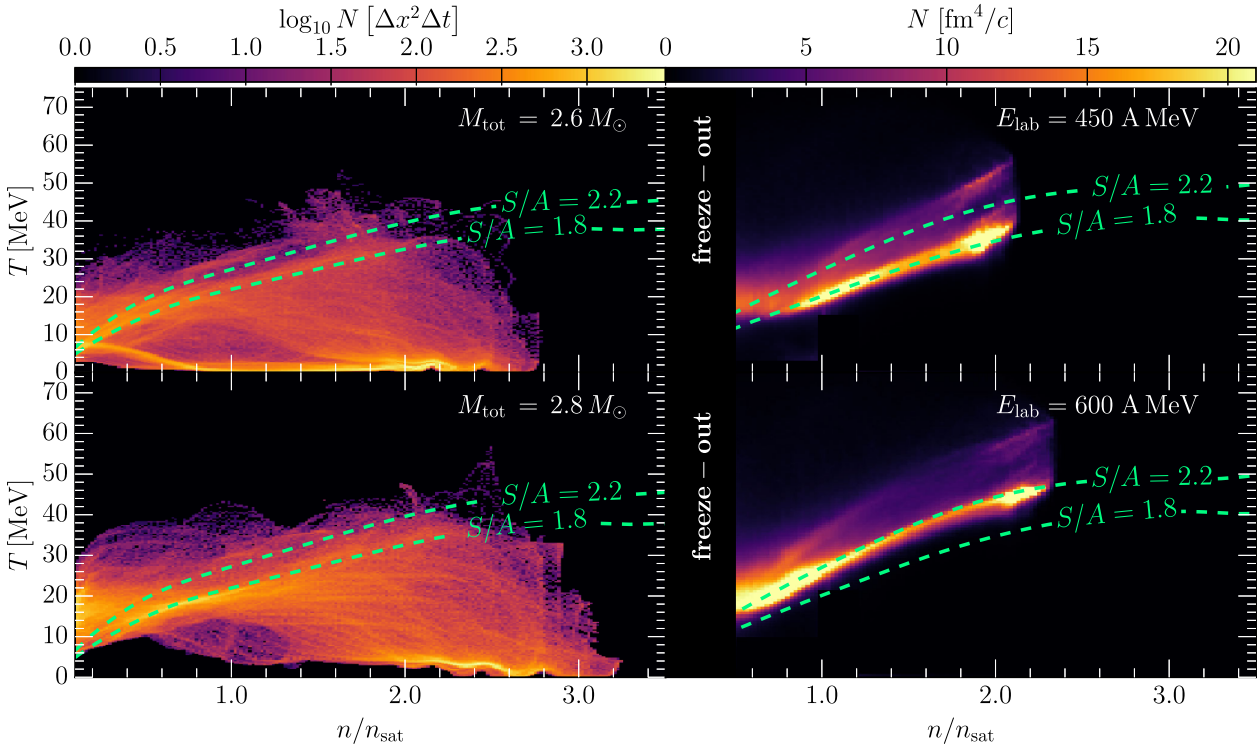

FIG. 4. Regions of the QCD phase-diagram probed by two BNSMs with different masses (left panels) and by two HICs with different beam energies (right panels). The color code reports the number of cells N in the various spacetimes having a given value of temperature and density. The green lines show contours of constant entropy per baryon. Only cells with density above freeze-out, $n > \frac{1}{2} n_{\rm sat}$, are shown for the HICs. In the BNSM case, we only consider the equatorial plane and normalize to arbitrary units.

to be representative of the overall dynamics, thus performing a $2+1$ binning; for the HIC, the full $3+1$ dynamics is used. For BNSs, we normalize to arbitrary units, since we are only interested in relative differences between populations of points in the phase diagram. We show the results of two distinct merger simulations differing in their total respective masses, namely, for a binary with $M_{\rm tot} = 2.6M_\odot$ (top left panel) and $2.8M_\odot$ (bottom left panel). For HICs, instead, we show the results at two different beam (kinetic) energies, namely at $E_{\rm lab} = 450A$ MeV (top right panel) and at $600A$ MeV (bottom right panel).

The left panel of Fig. 4 shows a broad range of densities, $n \lesssim 3.4 n_{\rm sat}$ and temperatures, $T \lesssim 40$ MeV covered by BNSMs. Two distinct regions appear in the phase diagram during and after the merger: the first is at high densities, $n > 2n_{\rm sat}$, and low temperatures, $T \lesssim 10$ MeV. This region corresponds to the central regions of the initial stars and the core of the postmerger remnant. As we have seen in Fig. 3, the neutron-star matter in this region does not undergo shock heating, but remains cold and with low entropies. Indeed, the oscillations seen at the lowest temperatures correspond to quadrupolar postmerger oscillations of the gravitationally bound rotating remnant [141]. This kind of matter is similar to cold stable neutron stars. The second region spanned by BNSMs in the phase diagram corresponds, instead, to hot matter with $T \gtrsim 10$ MeV and isentropes of $S/A = [1.8, 2.2]$, which were previously identified with the hot ring in the discussion of collision-shock dynamics (Fig. 3).

The distributions in the left panels of Fig. 4 clearly indicate that the lower mass binary populates regions with lower densities and temperatures ($n \lesssim n_{\rm sat}$, $T \lesssim 10$ MeV), which are essentially void in the case of the high-mass binary (see dark region around $n \sim \frac{1}{2} n_{\rm sat}$). On the other hand, low-density, high-temperature regions ($n \lesssim n_{\rm sat}$, $T \lesssim 30$ MeV) are highly populated for the case of the high-mass binary (see bright region around $n \lesssim 0.2 n_{\rm sat}$). Although the BNM evolution cannot be described as isentropic, interestingly, for both BNS masses, the regions corresponding to similar isentropes of $S/A \approx 2$ are populated. This range of entropies can be considered as characteristic for the hot matter probed in BNSs mergers and low-energy HICs. Because in our CMF model a significant quark fraction can only build up at densities $n_{\rm b} \gtrsim 3 n_{\rm sat}$ for the low temperatures reached in both BNSs and HICs, $T \lesssim 80$ MeV, no deconfined matter is expected in these.

The right panels of Fig. 4 show the same as in the left but for two HICs whose beam energies have been selected to provide a distribution in phase diagram comparable to that of a BNSM, namely, $E_{\rm lab} = 450A$ MeV and $600A$ MeV. Differently from the BNSMs, the evolution of HIC remnants after the initial collision is an almost isentropic expansion that populates the isentropes at $S/A \sim 2$. Clearly, different beam energies populate isentropes at lower/higher values of S/A (top/bottom panels). The rapid expansion from right to left along the isentrope continues until matter becomes too dilute to maintain local equilibrium and freezes out at $n \approx \frac{1}{2} n_{\rm sat}$.

The quite similar trajectories of the BNSM and the HICs in the QCD phase diagram (concerning temperature, density, and entropy per baryon) may appear surprising at first sight. We recall that the nuclei used in HICs consist of an almost equal number of neutrons and protons (and among their parity partners), corresponding to nearly isospin-symmetric matter, i.e., $Y_{\rm iso} \simeq -0.1$. Neutron-star matter is charge-neutral before the merger, consisting mainly of neutrons with a small admixture of protons, hyperons, parity partners, electrons, and muons in beta-equilibrium, i.e., $[-0.5 \lesssim Y_{\rm iso} \lesssim -0.4]$ (see, e.g., [52,140,142,143] for a more detailed discussion in the BNS-merger case). Nevertheless, these two different regimes are connected, and their relation is constrained at and around saturation density by the measurement of the (isospin) symmetry energy and its slope [144]. It should be made clear that the knowledge on how the EoS changes with isospin is an essential ingredient for the comparison for the two systems and is exactly the reason why a consistent comparison can only be made on the basis of a single model.

IV. CONCLUSIONS

In this work, we have set out to understand how well low-energy HICs are able to produce BNSM-like conditions [19]. To this end, we have performed a set of numerical simulations modeling both low-energy HICs and BNSMs, so that we can directly compare the geometry and thermodynamic conditions present in each system. We have carefully designed the study to use the same microphysics, i.e., the same EoS, and comparable numerical methods to solve the relativistic hydrodynamics problem in flat and dynamically curved spacetime. In order to mitigate a comparison of the very different flow structures in the presence of high net-angular momentum and strong gravity (for BNSMs), we have considered the local thermodynamic conditions probed. In particular, we have used the entropy production from shock heating at the initial impact as the figure of merit to meaningfully compare the two systems. The main result of this comparison, is the use of $S/A = [1.8, 2.2]$ isentropes to construct a mapping between gravitational masses of BNSs, i.e., $M_{\rm tot} = 2.6$–$2.8 M_\odot$, and the beam energies of heavy-ion experiments conducted in laboratories, i.e., $E_{\rm lab}/A = [450, 600]$ MeV [17]. HICs at these beam energies are currently being investigated by the HADES experiment at the SIS18 accelerator of GSI.

This analysis can be extended in several ways. While the overall error of neglecting viscous effects is likely be small in terms of the entropy production due to shock heating, a consistent study incorporating microphysical viscosity in the HIC [106,145–150] and BNSM [114,115,151] case would be desirable. In order to clarify uncertainties of the

cold EoS on the entropy production in both systems, further studies will be required, once more EoSs covering the relevant phase space, such as ours, become widely available. Our results present a significant step forward in the understanding of how well low-energy HICs can probe BNSM-like conditions. We expect these to be particularly useful for the interpretation of hot-dense matter reported to be formed in low-energy HICs [19], even more so, should future gravitational wave detectors be able to provide independent constraints on the hot dense matter EoS [58–60].

ACKNOWLEDGMENTS

The authors thank M. Alford, T. Galatyuk, J. Noronha-Hostler, and C. Raithel for insightful discussions and comments. E. R. M. gratefully acknowledges support as the John A. Wheeler fellow at the Princeton Center for Theoretical Science, and through fellowships at the Princeton Gravity Initiative, and the Institute for Advanced Study. A. M. acknowledges the Stern-Gerlach Postdoctoral fellowship of the Stiftung Polytechnische Gesellschaft. J. S. thank the Samson AG and the BMBF through the ErUM-Data project for funding. V. D. acknowledges support from the National Science Foundation under Grants No. PHY1748621, No. NP3M PHY-2116686, and No. MUSES OAC-2103680. L. R. acknowledges funding by the State of Hesse within the Research Cluster ELEMENTS (Project ID 500/10.006), by the ERC Advanced Grant "JETSET: Launching, propagation and emission of relativistic jets from binary mergers and across mass scales" (Grant No. 884631), and by HGS-HIRe for FAIR. H. S. acknowledges the Walter Greiner Gesellschaft zur Förderung der physikalischen Grundlagenforschung e.V. through the Judah M. Eisenberg Laureatus Chair at Goethe Universität.

[1] K. Rajagopal, Mapping the QCD phase diagram, Nucl. Phys. **A661**, 150 (1999).
[2] M. G. Alford, QCD at high density/temperature, Nucl. Phys. B, Proc. Suppl. **117**, 65 (2003).
[3] M. Buballa, NJL model analysis of quark matter at large density, Phys. Rep. **407**, 205 (2005).
[4] T. Schäfer, Quark matter, in *14th National Nuclear Physics Summer School* (2003), pp. 185–233, arXiv:hep-ph/0304281.
[5] K. Fukushima and T. Hatsuda, The phase diagram of dense QCD, Rep. Prog. Phys. **74**, 014001 (2011).
[6] U. Heinz and M. Jacob, Evidence for a new state of matter: An assessment of the results from the CERN lead beam programme, arXiv:nucl-th/0002042.
[7] I. Arsene *et al.* (BRAHMS Collaboration), Quark gluon plasma and color glass condensate at RHIC? The perspective from the BRAHMS experiment, Nucl. Phys. **A757**, 1 (2005).
[8] K. Adcox *et al.* (PHENIX Collaboration), Formation of dense partonic matter in relativistic nucleus-nucleus collisions at RHIC: Experimental evaluation by the PHENIX Collaboration, Nucl. Phys. **A757**, 184 (2005).
[9] B. B. Back *et al.* (PHOBOS Collaboration), The PHOBOS perspective on discoveries at RHIC, Nucl. Phys. **A757**, 28 (2005).
[10] J. Adams *et al.* (STAR Collaboration), Experimental and theoretical challenges in the search for the quark gluon plasma: The STAR Collaboration's critical assessment of the evidence from RHIC collisions, Nucl. Phys. **A757**, 102 (2005).
[11] S. Borsanyi, Z. Fodor, C. Hoelbling, S. D. Katz, S. Krieg, and K. K. Szabo, Full result for the QCD equation of state with $2+1$ flavors, Phys. Lett. B **730**, 99 (2014).
[12] A. Bazavov *et al.* (HotQCD Collaboration), Equation of state in $(2+1)$-flavor QCD, Phys. Rev. D **90**, 094503 (2014).
[13] A. Bazavov *et al.*, The QCD equation of state to $\mathcal{O}(\mu_B^6)$ from lattice QCD, Phys. Rev. D **95**, 054504 (2017).
[14] M. Gazdzicki (NA61/SHINE Collaboration), Ion program of NA61/Shine at the CERN SPS, J. Phys. G **36**, 064039 (2009).
[15] G. Agakishiev *et al.* (HADES Collaboration), The high-acceptance dielectron spectrometer HADES, Eur. Phys. J. A **41**, 243 (2009).
[16] K. Grebieszkow (NA61/SHINE Collaboration), New results on spectra and fluctuations from NA61/SHINE, Proc. Sci. CORFU2018 (**2019**) 152 [arXiv:1904.03165].
[17] T. Ablyazimov *et al.* (CBM Collaboration), Challenges in QCD matter physics–The scientific programme of the compressed baryonic matter experiment at FAIR, Eur. Phys. J. A **53**, 60 (2017).
[18] A. Bzdak, S. Esumi, V. Koch, J. Liao, M. Stephanov, and N. Xu, Mapping the phases of quantum chromodynamics with beam energy scan, Phys. Rep. **853**, 1 (2020).
[19] J. Adamczewski-Musch *et al.* (HADES Collaboration), Probing dense baryon-rich matter with virtual photons, Nat. Phys. **15**, 1040 (2019).
[20] S. Acharya *et al.* (ALICE Collaboration), Global baryon number conservation encoded in net-proton fluctuations measured in Pb-Pb collisions at $\sqrt{s_{\rm NN}} = 2.76$ TeV, Phys. Lett. B **807**, 135564 (2020).
[21] M. Abdallah *et al.* (STAR Collaboration), Cumulants and correlation functions of net-proton, proton, and antiproton multiplicity distributions in Au + Au collisions at energies available at the BNL relativistic heavy ion collider, Phys. Rev. C **104**, 024902 (2021).
[22] M. Abdallah *et al.* (STAR Collaboration), Measurement of the Sixth-Order Cumulant of Net-Proton Multiplicity Distributions in Au + Au Collisions at $\sqrt{s_{NN}} = 27$, 54.4, and 200 GeV at RHIC, Phys. Rev. Lett. **127**, 262301 (2021).

[23] B. P. Abbott *et al.* (LIGO Scientific and Virgo Collaborations), GW170817: Observation of Gravitational Waves from a Binary Neutron Star Inspiral, Phys. Rev. Lett. **119**, 161101 (2017).
[24] B. Margalit and B. D. Metzger, Constraining the maximum mass of neutron stars from multi-messenger observations of GW170817, Astrophys. J. Lett. **850**, L19 (2017).
[25] L. Rezzolla, E. R. Most, and L. R. Weih, Using gravitational-wave observations and quasi-universal relations to constrain the maximum mass of neutron stars, Astrophys. J. Lett. **852**, L25 (2018).
[26] M. Ruiz, S. L. Shapiro, and A. Tsokaros, GW170817, General relativistic magnetohydrodynamic simulations, and the neutron star maximum mass, Phys. Rev. D **97**, 021501 (2018).
[27] M. Shibata, E. Zhou, K. Kiuchi, and S. Fujibayashi, Constraint on the maximum mass of neutron stars using GW170817 event, Phys. Rev. D **100**, 023015 (2019).
[28] E. Annala, T. Gorda, A. Kurkela, and A. Vuorinen, Gravitational-Wave Constraints on the Neutron-Star-Matter Equation of State, Phys. Rev. Lett. **120**, 172703 (2018).
[29] D. Radice, A. Perego, F. Zappa, and S. Bernuzzi, GW170817: Joint constraint on the neutron star equation of state from multimessenger observations, Astrophys. J. Lett. **852**, L29 (2018).
[30] A. Bauswein, O. Just, H.-T. Janka, and N. Stergioulas, Neutron-star radius constraints from GW170817 and future detections, Astrophys. J. Lett. **850**, L34 (2017).
[31] E. R. Most, L. R. Weih, L. Rezzolla, and J. Schaffner-Bielich, New Constraints on Radii and Tidal Deformabilities of Neutron Stars from GW170817, Phys. Rev. Lett. **120**, 261103 (2018).
[32] B. P. Abbott *et al.* (LIGO Scientific and Virgo Collaborations), GW170817: Measurements of Neutron Star Radii and Equation of State, Phys. Rev. Lett. **121**, 161101 (2018).
[33] C. Raithel, F. Özel, and D. Psaltis, Tidal deformability from GW170817 as a direct probe of the neutron star radius, Astrophys. J. Lett. **857**, L23 (2018).
[34] S. De, D. Finstad, J. M. Lattimer, D. A. Brown, E. Berger, and C. M. Biwer, Tidal Deformabilities and Radii of Neutron Stars from the Observation of GW170817, Phys. Rev. Lett. **121**, 091102 (2018); **121**, 259902(E) (2018).
[35] K. Chatziioannou, C.-J. Haster, and A. Zimmerman, Measuring the neutron star tidal deformability with equation-of-state-independent relations and gravitational waves, Phys. Rev. D **97**, 104036 (2018).
[36] Z. Carson, A. W. Steiner, and K. Yagi, Constraining nuclear matter parameters with GW170817, Phys. Rev. D **99**, 043010 (2019).
[37] V. Dexheimer, R. de Oliveira Gomes, S. Schramm, and H. Pais, What do we learn about vector interactions from GW170817?, J. Phys. G **46**, 034002 (2019).
[38] Y. Lim and J. W. Holt, Bayesian modeling of the nuclear equation of state for neutron star tidal deformabilities and GW170817, Eur. Phys. J. A **55**, 209 (2019).
[39] R. Essick, P. Landry, and D. E. Holz, Nonparametric inference of neutron star composition, equation of state, and maximum mass with GW170817, Phys. Rev. D **101**, 063007 (2020).
[40] E. R. Most, L. J. Papenfort, L. R. Weih, and L. Rezzolla, A lower bound on the maximum mass if the secondary in GW190814 was once a rapidly spinning neutron star, Mon. Not. R. Astron. Soc. **499**, L82 (2020).
[41] H. Tan, J. Noronha-Hostler, and N. Yunes, Neutron Star Equation of State in light of GW190814, Phys. Rev. Lett. **125**, 261104 (2020).
[42] H. Tan, T. Dore, V. Dexheimer, J. Noronha-Hostler, and N. Yunes, Extreme matter meets extreme gravity: Ultraheavy neutron stars with phase transitions, Phys. Rev. D **105**, 023018 (2022).
[43] H. Tan, V. Dexheimer, J. Noronha-Hostler, and N. Yunes, The Slope, the Hill, the Drop, and the Swoosh: Learning About the Nuclear Matter Equation of State from the Binary Love Relations, Phys. Rev. Lett. **128**, 161101 (2022).
[44] A. Nathanail, E. R. Most, and L. Rezzolla, GW170817 and GW190814: Tension on the maximum mass, Astrophys. J. Lett. **908**, L28 (2021).
[45] P. Danielewicz, R. Lacey, and W. G. Lynch, Determination of the equation of state of dense matter, Science **298**, 1592 (2002).
[46] W. G. Lynch, M. B. Tsang, Y. Zhang, P. Danielewicz, M. Famiano, Z. Li, and A. W. Steiner, Probing the symmetry energy with heavy ions, Prog. Part. Nucl. Phys. **62**, 427 (2009).
[47] S. Huth *et al.*, Constraining neutron-star matter with microscopic and macroscopic collisions, Nature (London) **606**, 276 (2022).
[48] R. Oechslin, K. Uryu, G. S. Poghosyan, and F. K. Thielemann, The influence of quark matter at high densities on binary neutron star mergers, Mon. Not. R. Astron. Soc. **349**, 1469 (2004).
[49] S. Bose, K. Chakravarti, L. Rezzolla, B. S. Sathyaprakash, and K. Takami, Neutron-Star Radius from a Population of Binary Neutron Star Mergers, Phys. Rev. Lett. **120**, 031102 (2018).
[50] E. R. Most, L. J. Papenfort, V. Dexheimer, M. Hanauske, S. Schramm, H. Stöcker, and L. Rezzolla, Signatures of Quark-Hadron Phase Transitions in General-Relativistic Neutron-Star Mergers, Phys. Rev. Lett. **122**, 061101 (2019).
[51] A. Bauswein, N.-U. F. Bastian, D. B. Blaschke, K. Chatziioannou, J. A. Clark, T. Fischer, and M. Oertel, Identifying a First-Order Phase Transition in Neutron Star Mergers Through Gravitational Waves, Phys. Rev. Lett. **122**, 061102 (2019).
[52] E. R. Most, L. Jens Papenfort, V. Dexheimer, M. Hanauske, H. Stoecker, and L. Rezzolla, On the deconfinement phase transition in neutron-star mergers, Eur. Phys. J. A **56**, 59 (2020).
[53] L. R. Weih, M. Hanauske, and L. Rezzolla, Postmerger Gravitational-Wave Signatures of Phase Transitions in Binary Mergers, Phys. Rev. Lett. **124**, 171103 (2020).
[54] S. L. Liebling, C. Palenzuela, and L. Lehner, Effects of high density phase transitions on neutron star dynamics, Classical Quantum Gravity **38**, 115007 (2021).
[55] A. Prakash, D. Radice, D. Logoteta, A. Perego, V. Nedora, I. Bombaci, R. Kashyap, S. Bernuzzi, and A. Endrizzi, Signatures of deconfined quark phases in binary neutron star mergers, Phys. Rev. D **104**, 083029 (2021).

[56] S. Tootle, C. Ecker, K. Topolski, T. Demircik, M. Järvinen, and L. Rezzolla, Quark formation and phenomenology in binary neutron-star mergers using V-QCD, SciPost Phys. **13**, 109 (2022).
[57] Y.-J. Huang, L. Baiotti, T. Kojo, K. Takami, H. Sotani, H. Togashi, T. Hatsuda, S. Nagataki, and Y.-Z. Fan, Merger and Postmerger of Binary Neutron Stars with a Quark-Hadron Crossover Equation of State, Phys. Rev. Lett. **129**, 181101 (2022).
[58] M. Punturo *et al.*, The Einstein Telescope: A third-generation gravitational wave observatory, Classical Quantum Gravity **27**, 194002 (2010).
[59] D. Reitze *et al.*, Cosmic explorer: The U.S. contribution to gravitational-wave astronomy beyond LIGO, Bull. Am. Astron. Soc. **51**, 035 (2019).
[60] K. Ackley *et al.*, Neutron star extreme matter observatory: A kilohertz-band gravitational-wave detector in the global network, Pub. Astron. Soc. Aust. **37**, e047 (2020).
[61] G. Raaijmakers, S. K. Greif, K. Hebeler, T. Hinderer, S. Nissanke, A. Schwenk, T. E. Riley, A. L. Watts, J. M. Lattimer, and W. C. G. Ho, Constraints on the dense matter equation of state and neutron star properties from NICER's mass–Radius estimate of PSR J0740 + 6620 and multi-messenger observations, Astrophys. J. Lett. **918**, L29 (2021).
[62] M. C. Miller *et al.*, The radius of PSR J0740 + 6620 from NICER and XMM-Newton data, Astrophys. J. Lett. **918**, L28 (2021).
[63] M. Fasano, T. Abdelsalhin, A. Maselli, and V. Ferrari, Constraining the Neutron Star Equation of State Using Multiband Independent Measurements of Radii and Tidal Deformabilities, Phys. Rev. Lett. **123**, 141101 (2019).
[64] A. Bauswein, N.-U. Friedrich Bastian, D. Blaschke, K. Chatziioannou, J. A. Clark, T. Fischer, H.-T. Janka, O. Just, M. Oertel, and N. Stergioulas, Equation-of-state constraints and the QCD phase transition in the era of gravitational-wave astronomy, AIP Conf. Proc. **2127**, 020013 (2019).
[65] C. D. Capano, I. Tews, S. M. Brown, B. Margalit, S. De, S. Kumar, D. A. Brown, B. Krishnan, and S. Reddy, Stringent constraints on neutron-star radii from multimessenger observations and nuclear theory, Nat. Astron. **4**, 625 (2020).
[66] T. Dietrich, M. W. Coughlin, P. T. H. Pang, M. Bulla, J. Heinzel, L. Issa, I. Tews, and S. Antier, Multimessenger constraints on the neutron-star equation of state and the Hubble constant, Science **370**, 1450 (2020).
[67] P. Landry, R. Essick, and K. Chatziioannou, Nonparametric constraints on neutron star matter with existing and upcoming gravitational wave and pulsar observations, Phys. Rev. D **101**, 123007 (2020).
[68] M. Al-Mamun, A. W. Steiner, J. Nättilä, J. Lange, R. O'Shaughnessy, I. Tews, S. Gandolfi, C. Heinke, and S. Han, Combining Electromagnetic and Gravitational-Wave Constraints on Neutron-Star Masses and Radii, Phys. Rev. Lett. **126**, 061101 (2021).
[69] Y. Zhou, L.-W. Chen, and Z. Zhang, Equation of state of dense matter in the multimessenger era, Phys. Rev. D **99**, 121301 (2019).
[70] N.-B. Zhang, B.-A. Li, and J. Xu, Combined constraints on the equation of state of dense neutron-rich matter from terrestrial nuclear experiments and observations of neutron stars, Astrophys. J. **859**, 90 (2018).
[71] P. G. Krastev and B.-A. Li, Imprints of the nuclear symmetry energy on the tidal deformability of neutron stars, J. Phys. G **46**, 074001 (2019).
[72] B. T. Reed, F. J. Fattoyev, C. J. Horowitz, and J. Piekarewicz, Implications of PREX-2 on the Equation of State of Neutron-Rich Matter, Phys. Rev. Lett. **126**, 172503 (2021).
[73] C. Y. Tsang, M. B. Tsang, P. Danielewicz, W. G. Lynch, and F. J. Fattoyev, Towards a better understanding of the symmetry energy within neutron stars, arXiv:1901.07673.
[74] B. Kumar, Neutron skins of heavy nuclei and tidal deformability of neutron star, J. Phys. Soc. Jpn. Conf. Proc. **31**, 011052 (2020).
[75] V. Sagun, I. Lopes, and A. Ivanytskyi, Neutron stars meet constraints from high and low energy nuclear physics, Nucl. Phys. **A982**, 883 (2019).
[76] B.-A. Li and W.-J. Xie, Symmetry energy of super-dense neutron-rich matter from integrating barotropic pressures in neutron stars and heavy-ion reactions, Phys. Lett. B **806**, 135517 (2020).
[77] J. J. Li, A. Sedrakian, and M. Alford, Relativistic hybrid stars in the light of NICER PSR J0740 + 6620 radius measurement, Phys. Rev. D **104**, L121302 (2021).
[78] B. Biswas, Impact of PREX-II and combined radio/NICER/XMM-Newton's mass–Radius measurement of PSR J0740 + 6620 on the dense-matter equation of state, Astrophys. J. **921**, 63 (2021).
[79] S. K. Biswal, H. C. Das, A. Kumar, and S. K. Patra, Constraining nuclear matter parameters and neutron star observables using PREX-2 and NICER data, arXiv:2109.11895.
[80] C. Drischler, S. Han, and S. Reddy, Large and massive neutron stars: Implications for the sound speed in dense QCD, Phys. Rev. C **105**, 035808 (2022).
[81] M. Ferreira and C. Providência, Constraints on high density equation of state from maximum neutron star mass, Phys. Rev. D **104**, 063006 (2021).
[82] G. Aarts, C. Allton, D. De Boni, S. Hands, B. Jäger, C. Praki, and J.-I. Skullerud, Light baryons below and above the deconfinement transition: Medium effects and parity doubling, J. High Energy Phys. 06 (2017) 034.
[83] E. S. Fraga, A. Kurkela, and A. Vuorinen, Interacting quark matter equation of state for compact stars, Astrophys. J. Lett. **781**, L25 (2014).
[84] N. Haque, A. Bandyopadhyay, J. O. Andersen, M. G. Mustafa, M. Strickland, and N. Su, Three-loop HTLpt thermodynamics at finite temperature and chemical potential, J. High Energy Phys. 05 (2014) 027.
[85] S. Pratt, E. Sangaline, P. Sorensen, and H. Wang, Constraining the Equation of State of Super-Hadronic Matter from Heavy-Ion Collisions, Phys. Rev. Lett. **114**, 202301 (2015).
[86] P. Papazoglou, D. Zschiesche, S. Schramm, J. Schaffner-Bielich, H. Stoecker, and W. Greiner, Nuclei in a chiral SU(3) model, Phys. Rev. C **59**, 411 (1999).

[87] V. Dexheimer and S. Schramm, Proto-neutron and neutron stars in a chiral SU(3) model, Astrophys. J. **683**, 943 (2008).
[88] A. Motornenko, J. Steinheimer, V. Vovchenko, S. Schramm, and H. Stoecker, Equation of state for hot QCD and compact stars from a mean field approach, Phys. Rev. C **101**, 034904 (2020).
[89] R. L. Workman *et al.* (Particle Data Group), Review of particle physics, Prog. Theor. Exp. Phys. **2022**, 083C01 (2022).
[90] D. H. Rischke, M. I. Gorenstein, H. Stoecker, and W. Greiner, Excluded volume effect for the nuclear matter equation of state, Z. Phys. C **51**, 485 (1991).
[91] K. Fukushima, Chiral effective model with the Polyakov loop, Phys. Lett. B **591**, 277 (2004).
[92] C. Ratti, M. A. Thaler, and W. Weise, Phases of QCD: Lattice thermodynamics and a field theoretical model, Phys. Rev. D **73**, 014019 (2006).
[93] J. Steinheimer, S. Schramm, and H. Stocker, An effective chiral hadron-quark equation of state part I: Zero baryochemical potential, arXiv:0909.4421.
[94] P. Zyla *et al.* (Particle Data Group), Review of particle physics, Prog. Theor. Exp. Phys. **2020**, 083C01 (2020).
[95] A. Motornenko, S. Pal, A. Bhattacharyya, J. Steinheimer, and H. Stoecker, Repulsive properties of hadrons in lattice QCD data and neutron stars, Phys. Rev. C **103**, 054908 (2021).
[96] A. S. Schneider, L. F. Roberts, and C. D. Ott, Open-source nuclear equation of state framework based on the liquid-drop model with Skyrme interaction, Phys. Rev. C **96**, 065802 (2017).
[97] A. Motornenko, V. Vovchenko, J. Steinheimer, S. Schramm, and H. Stoecker, QCD at high density: Equation of state for nuclear collisions and neutron stars, Nucl. Phys. **A982**, 891 (2019).
[98] A. Motornenko, J. Steinheimer, V. Vovchenko, S. Schramm, and H. Stoecker, Matter and gravitation in collisions of heavy ions and neutron stars: Equation of state, Proc. Sci. CORFU2018 (**2019**) 150 [arXiv:1907.05921].
[99] S. Altiparmak, C. Ecker, and L. Rezzolla, On the sound speed in neutron stars, Astrophys. J. Lett. **939**, L34 (2022).
[100] C. Ecker and L. Rezzolla, A general, scale-independent description of the sound speed in neutron stars, Astrophys. J. Lett. **939**, L35 (2022).
[101] S. Altiparmak, C. Ecker, and L. Rezzolla, On the sound speed in neutron stars, Astrophys. J. Lett. **939**, L34 (2022).
[102] J. A. Font, Numerical hydrodynamics in general relativity, Living Rev. Relativity **3**, 2 (2000).
[103] M. Omana Kuttan, A. Motornenko, J. Steinheimer, H. Stoecker, Y. Nara, and M. Bleicher, A chiral mean-field equation-of-state in UrQMD: Effects on the heavy ion compression stage, Eur. Phys. J. C **82**, 427 (2022).
[104] G. Inghirami and H. Elfner, The applicability of hydrodynamics in heavy ion collisions at $\sqrt{s_{\mathrm{NN}}} = 2.4$–$7.7$ GeV, Eur. Phys. J. C **82**, 796 (2022).
[105] H. Song and U. W. Heinz, Causal viscous hydrodynamics in $2+1$ dimensions for relativistic heavy-ion collisions, Phys. Rev. C **77**, 064901 (2008).
[106] P. Bozek, Bulk and shear viscosities of matter created in relativistic heavy-ion collisions, Phys. Rev. C **81**, 034909 (2010).
[107] I. Karpenko, P. Huovinen, and M. Bleicher, A $3+1$ dimensional viscous hydrodynamic code for relativistic heavy ion collisions, Comput. Phys. Commun. **185**, 3016 (2014).
[108] C. Shen, Z. Qiu, H. Song, J. Bernhard, S. Bass, and U. Heinz, The iEBE-VISHNU code package for relativistic heavy-ion collisions, Comput. Phys. Commun. **199**, 61 (2016).
[109] L.-G. Pang, H. Petersen, and X.-N. Wang, Pseudorapidity distribution and decorrelation of anisotropic flow within the open-computing-language implementation CLVisc hydrodynamics, Phys. Rev. C **97**, 064918 (2018).
[110] F. S. Bemfica, M. M. Disconzi, and J. Noronha, General-Relativistic Viscous Fluid Dynamics, Phys. Rev. X **12**, 021044 (2022).
[111] M. Chabanov, L. Rezzolla, and D. H. Rischke, General-relativistic hydrodynamics of non-perfect fluids: $3+1$ conservative formulation and application to viscous black hole accretion, Mon. Not. R. Astron. Soc. **505**, 5910 (2021).
[112] A. Pandya and F. Pretorius, Numerical exploration of first-order relativistic hydrodynamics, Phys. Rev. D **104**, 023015 (2021).
[113] E. R. Most and J. Noronha, Dissipative magnetohydrodynamics for nonresistive relativistic plasmas: An implicit second-order flux-conservative formulation with stiff relaxation, Phys. Rev. D **104**, 103028 (2021).
[114] E. R. Most, A. Haber, S. P. Harris, Z. Zhang, M. G. Alford, and J. Noronha, Emergence of microphysical viscosity in binary neutron star post-merger dynamics, arXiv:2207.00442.
[115] M. G. Alford, L. Bovard, M. Hanauske, L. Rezzolla, and K. Schwenzer, Viscous Dissipation and Heat Conduction in Binary Neutron-Star Mergers, Phys. Rev. Lett. **120**, 041101 (2018).
[116] L. Rezzolla and O. Zanotti, *Relativistic Hydrodynamics* (Oxford University Press, Oxford, 2013).
[117] J. P. Boris and D. L. Book, Flux-corrected transport. I. SHASTA, a fluid transport algorithm that works, J. Comput. Phys. **11**, 38 (1973).
[118] D. H. Rischke, S. Bernard, and J. A. Maruhn, Relativistic hydrodynamics for heavy ion collisions. 1. General aspects and expansion into vacuum, Nucl. Phys. **A595**, 346 (1995).
[119] D. Hilditch, S. Bernuzzi, M. Thierfelder, Z. Cao, W. Tichy, and B. Bruegmann, Compact binary evolutions with the Z4c formulation, Phys. Rev. D **88**, 084057 (2013).
[120] S. Bernuzzi and D. Hilditch, Constraint violation in free evolution schemes: Comparing BSSNOK with a conformal decomposition of Z4, Phys. Rev. D **81**, 084003 (2010).
[121] D. Alic, C. Bona-Casas, C. Bona, L. Rezzolla, and C. Palenzuela, Conformal and covariant formulation of the Z4 system with constraint-violation damping, Phys. Rev. D **85**, 064040 (2012).
[122] D. Alic, W. Kastaun, and L. Rezzolla, Constraint damping of the conformal and covariant formulation of the Z4 system in simulations of binary neutron stars, Phys. Rev. D **88**, 064049 (2013).
[123] Z. B. Etienne, V. Paschalidis, R. Haas, P. Mösta, and S. L. Shapiro, IllinoisGRMHD: An open-source, user-friendly

GRMHD code for dynamical spacetimes, Classical Quantum Gravity **32**, 175009 (2015).
[124] E. R. Most, L. J. Papenfort, and L. Rezzolla, Beyond second-order convergence in simulations of magnetized binary neutron stars with realistic microphysics, Mon. Not. R. Astron. Soc. **490**, 3588 (2019).
[125] F. Loffler *et al.*, The Einstein Toolkit: A community computational infrastructure for relativistic astrophysics, Classical Quantum Gravity **29**, 115001 (2012).
[126] E. Schnetter, S. H. Hawley, and I. Hawke, Evolutions in 3-D numerical relativity using fixed mesh refinement, Classical Quantum Gravity **21**, 1465 (2004).
[127] E. Gourgoulhon, P. Grandclement, K. Taniguchi, J.-A. Marck, and S. Bonazzola, Quasiequilibrium sequences of synchronized and irrotational binary neutron stars in general relativity: 1. Method and tests, Phys. Rev. D **63**, 064029 (2001).
[128] L. Bildsten and C. Cutler, Tidal interactions of inspiraling compact binaries, Astrophys. J. **400**, 175 (1992).
[129] P. Romatschke and U. Romatschke, *Relativistic Fluid Dynamics In and Out of Equilibrium: And Applications to Relativistic Nuclear Collisions*, Cambridge Monographs on Mathematical Physics (Cambridge University Press, Cambridge, England, 2019).
[130] M. Omana Kuttan, A. Motornenko, J. Steinheimer, H. Stoecker, Y. Nara, and M. Bleicher, A chiral mean-field equation-of-state in UrQMD: Effects on the heavy ion compression stage, Eur. Phys. J. C **82**, 427 (2022).
[131] L. Baiotti and L. Rezzolla, Binary neutron star mergers: A review of Einstein's richest laboratory, Rep. Prog. Phys. **80**, 096901 (2017).
[132] F. Hofmann, E. Barausse, and L. Rezzolla, The final spin from binary black holes in quasi-circular orbits, Astrophys. J. Lett. **825**, L19 (2016).
[133] L. Baiotti, B. Giacomazzo, and L. Rezzolla, Accurate evolutions of inspiralling neutron-star binaries: Prompt and delayed collapse to black hole, Phys. Rev. D **78**, 084033 (2008).
[134] M. Hanauske, K. Takami, L. Bovard, L. Rezzolla, J. A. Font, F. Galeazzi, and H. Stöcker, Rotational properties of hypermassive neutron stars from binary mergers, Phys. Rev. D **96**, 043004 (2017).
[135] W. Kastaun, R. Ciolfi, and B. Giacomazzo, Structure of stable binary neutron star merger remnants: A case study, Phys. Rev. D **94**, 044060 (2016).
[136] P. Arras and N. N. Weinberg, Urca reactions during neutron star inspiral, Mon. Not. R. Astron. Soc. **486**, 1424 (2019).
[137] J. S. Read, L. Baiotti, J. D. E. Creighton, J. L. Friedman, B. Giacomazzo, K. Kyutoku, C. Markakis, L. Rezzolla, M. Shibata, and K. Taniguchi, Matter effects on binary neutron star waveforms, Phys. Rev. D **88**, 044042 (2013).
[138] K. Takami, L. Rezzolla, and L. Baiotti, Spectral properties of the post-merger gravitational-wave signal from binary neutron stars, Phys. Rev. D **91**, 064001 (2015).
[139] M. Hanauske, J. Steinheimer, L. Bovard, A. Mukherjee, S. Schramm, K. Takami, J. Papenfort, N. Wechselberger, L. Rezzolla, and H. Stöcker, Concluding remarks: Connecting relativistic heavy ion collisions and neutron star mergers by the equation of state of dense hadron- and quark matter as signalled by gravitational waves, J. Phys. Conf. Ser. **878**, 012031 (2017).
[140] E. R. Most and C. A. Raithel, Impact of the nuclear symmetry energy on the post-merger phase of a binary neutron star coalescence, Phys. Rev. D **104**, 124012 (2021).
[141] L. Rezzolla and K. Takami, Gravitational-wave signal from binary neutron stars: A systematic analysis of the spectral properties, Phys. Rev. D **93**, 124051 (2016).
[142] P. Hammond, I. Hawke, and N. Andersson, Thermal aspects of neutron star mergers, Phys. Rev. D **104**, 103006 (2021).
[143] A. Perego, S. Bernuzzi, and D. Radice, Thermodynamics conditions of matter in neutron star mergers, Eur. Phys. J. A **55**, 124 (2019).
[144] M. B. Tsang, Y. Zhang, P. Danielewicz, M. Famiano, Z. Li, W. G. Lynch, and A. W. Steiner, Constraints on the Density Dependence of the Symmetry Energy, Phys. Rev. Lett. **102**, 122701 (2009).
[145] A. Monnai and T. Hirano, Effects of bulk viscosity at freezeout, Phys. Rev. C **80**, 054906 (2009).
[146] H. Song and U. W. Heinz, Interplay of shear and bulk viscosity in generating flow in heavy-ion collisions, Phys. Rev. C **81**, 024905 (2010).
[147] K. Dusling and T. Schäfer, Bulk viscosity, particle spectra and flow in heavy-ion collisions, Phys. Rev. C **85**, 044909 (2012).
[148] J. Noronha-Hostler, G. S. Denicol, J. Noronha, R. P. G. Andrade, and F. Grassi, Bulk viscosity effects in event-by-event relativistic hydrodynamics, Phys. Rev. C **88**, 044916 (2013).
[149] S. Ryu, J. F. Paquet, C. Shen, G. S. Denicol, B. Schenke, S. Jeon, and C. Gale, Importance of the Bulk Viscosity of QCD in Ultrarelativistic Heavy-Ion Collisions, Phys. Rev. Lett. **115**, 132301 (2015).
[150] S. Ryu, J.-F. Paquet, C. Shen, G. Denicol, B. Schenke, S. Jeon, and C. Gale, Effects of bulk viscosity and hadronic rescattering in heavy ion collisions at energies available at the BNL relativistic heavy ion collider and at the CERN large hadron collider, Phys. Rev. C **97**, 034910 (2018).
[151] E. R. Most, S. P. Harris, C. Plumberg, M. G. Alford, J. Noronha, J. Noronha-Hostler, F. Pretorius, H. Witek, and N. Yunes, Projecting the likely importance of weak-interaction-driven bulk viscosity in neutron star mergers, Mon. Not. R. Astron. Soc. **509**, 1096 (2021).